Generation of the Jovian hectometric radiation: First lessons from Juno

J. L. Zink, R. J. Wilson, S. Weidner, J. R. Szalay, S. Levin, M. Imai, R. W. Ebert, J. Connerney, S. Bolton, F. Bagenal, et al.

AGU PUBLICATIONS

Geophysical Research Letters

RESEARCH LETTER
10.1002/2017GL072923

Special Section:
Early Results: Juno at Jupiter

Generation of the Jovian hectometric radiation: First lessons from Juno

P. Louarn[1], F. Allegrini[2,3], D. J. McComas[2,8], P. W. Valek[2,3], W. S. Kurth[4], N. André[1], F. Bagenal[5], S. Bolton[2], J. Connerney[6], R. W. Ebert[2], M. Imai[4], S. Levin[7], J. R. Szalay[2], S. Weidner[8], R. J. Wilson[5], and J. L. Zink[2]

[1]Institut de Recherche en Astrophysique et Planétologie, Toulouse, France, [2]Southwest Research Institute, San Antonio, Texas, USA, [3]Department of Physics and Astronomy, University of Texas at San Antonio, San Antonio, Texas, USA, [4]University of Iowa, Iowa City, Iowa, USA, [5]Laboratory for Atmospheric and Space Physics, University of Colorado Boulder, Boulder, Colorado, USA, [6]NASA Goddard Space Flight Center, Greenbelt, Maryland, USA, [7]Jet Propulsion Laboratory, Pasadena, California, USA, [8]Department of Astrophysical Sciences, Princeton University, Princeton, New Jersey, USA

Key Points:
- First detailed wave/particle investigation in a Jovian radio source, using JADE, Waves, and MAG Juno instruments
- Confirmation that the cyclotron maser instability is the generation mechanism
- Demonstration that the observed loss cone distributions provide sufficient growth rates to explain the wave amplification

Correspondence to:
P. Louarn,
philippe.louarn@irap.omp.eu

Citation:
Louarn, P., et al. (2017), Generation of the Jovian hectometric radiation: First lessons from Juno, *Geophys. Res. Lett.*, *44*, 4439–4446, doi:10.1002/2017GL072923.

Received 6 FEB 2017
Accepted 8 MAR 2017
Published online 25 MAY 2017

Abstract Using Juno plasma and wave and magnetic observations (JADE and Waves and MAG instruments), the generation mechanism of the Jovian hectometric radio emission is analyzed. It is shown that suitable conditions for the cyclotron maser instability (CMI) are observed in the regions of the radio sources. Pronounced loss cone in the electron distributions are likely the source of free energy for the instability. The theory reveals that sufficient growth rates are obtained from the distribution functions that are measured by the JADE-Electron instrument. The CMI would be driven by upgoing electron populations at 5–10 keV and 10–30° pitch angle, the amplified waves propagating at 82°–87° from the *B* field, a fraction of a percent above the gyrofrequency. Typical *e*-folding times of 10^{-4} s are obtained, leading to an amplification path of ~1000 km. Overall, this scenario for generation of the Jovian hectometric waves differs significantly from the case of the auroral kilometric radiation at Earth.

1. Introduction

Juno crossed Jupiter's polar regions on 27 August 2016 and performed the first plasma and wave measurements in the low-altitude auroral regions of Jupiter (see *Bagenal et al.* [2014], for review of Juno's magnetospheric objectives). This constitutes the first opportunity to directly investigate in situ the properties of the Jovian auroral radio emissions and measure the features of the electron populations that may be responsible for their generation. Analysis at similar levels of detail was only possible at Earth with spinning spacecraft such as S3-3, Viking, and FAST [*Omidi et al.*, 1984; *Roux et al.*, 1993; *Ergun et al.*, 1998]. The other unique example of extraterrestrial source crossing was at Saturn with Cassini [*Lamy et al.*, 2010]. One objective of this exploration is to understand the scenario for generation of one of the most powerful nonthermal radio emissions in the solar system, well explored since the dawn of radio astronomy [*Burke and Franklin*, 1955] by professional and amateur observers. Such a scenario is likely of general astrophysical use [*Melrose and Dulk*, 1982].

It is now widely recognized that the cyclotron maser instability (CMI) is the generation mechanism of the nonthermal auroral radio emissions (see *Wu* [1985] for a review). A large number of theoretical studies and observations support this mechanism (see *Zarka* [1998] for a review). The CMI indeed appears to be particularly capable of the amplification of *X*-mode waves at frequencies close to the electron gyrofrequency in a tenuous plasma ($\varepsilon = (f_p/f_c)^2 \ll 1$ where f_p and f_c are respectively the electron plasma and gyrofrequency) provided that the electron distribution presents positive $\partial f/\partial v_\perp$ gradients ($v_\perp$ is the velocity perpendicular to the static *B* field). These are very general features of the electron velocity distributions observed in the auroral regions which is why the CMI theory is widely successful.

The application of CMI theory is well established at Earth. It has been demonstrated that the auroral kilometric radiation (AKR) is generated in relatively small regions (a few tens of kilometers in the direction perpendicular to the *B* field), corresponding to acceleration regions that are magnetically connected to the aurora [*Louarn et al.*, 1990; *Delory et al.*, 1998]. These localized regions of very low density are characterized by electron distributions presenting a bump at large pitch angles (the "trapped" or "horseshoe" population). This led people to consider CMI regimes that are different than the one initially proposed by *Wu and Lee*

[1979]. Indeed, since the plasma in the sources is dominated by electrons at keV energies, the gyrofrequency is decreased due to the relativistic effect ($\Delta f_c/f_c \sim E/m_e c^2$, where E is the typical electron kinetic energy). This allows one to use free energy at ~90° pitch angle, in the case of strictly perpendicular propagation. This is a particularly efficient CMI regime [*Pritchett*, 1986; *Le Quéau and Louarn*, 1989; *Louarn et al*., 1990].

An obvious question is to investigate whether the AKR scenario applies at Jupiter or if other CMI regimes need to be considered. We use measurements performed by the Juno plasma instrument: JADE [*McComas et al*., 2013]; radio and wave instrument: Waves (see *Kurth et al*. [2017] for details on Waves); and magnetometer: MAG [*Connerney et al*., 2017], to investigate the Jovian generation mechanisms. We refer to *Allegrini et al*. [2017] and *Szalay et al*. [2017] to present the details of JADE-E observations performed in the auroral regions during PJ1. The present investigation also relies on *Kurth et al*. [2017] which presents an overview of the first Juno radio observations, with descriptions of several close approaches or crossings of radio sources regions.

In this study we concentrate on the analysis of the source of hectometric radiation (HOM) labeled "C" in *Kurth et al*. [2017], crossed at ~13:29 UT on 27 August 2016. In particular, we calculate the CMI growth rates using distribution functions that are measured by JADE-E and obtain positive results. Obtaining sufficiently large growth rates from measured distributions does not occur as frequently as one may think. Even with the highest time resolution measurements made at Earth, the measured $\partial f/\partial v_\perp$ gradients are rarely sufficient to explain the wave generation due to the nonlinear wave-particle diffusion rapidly eroding the available free energy.

2. Observations

In Figure 1, we show the wave and particle observations obtained during a possible crossing of HOM source, in the southern hemisphere. The region corresponds to the source labeled C in Figure 4 of *Kurth et al*. [2017]. This time period is also discussed in *Szalay et al*. [2017] and *Allegrini et al*. [2017]. These papers provide the magnetospheric context of these observations and show that at 13:29:00–13:29:30 Juno transitioned from being magnetically connected to the inner plasma sheet to the outer plasma sheet (~30–40 Jovian radius (R_J)).

In Figure 1a, the wave dynamic spectra from 4 to 10 MHz are shown. The significant increase of the wave flux at or very close to the local gyrofrequency (white line in Figure 1a), occurring from ~13:28 to 13:29:45, can be considered a signature of crossing a CMI source. The maximum flux is about an order of magnitude larger than in the adjacent regions. The close proximity of the strong emission to the local gyrofrequency indicates that the ratio between the plasma and the gyrofrequency is very small ($\omega_p/\omega_c \ll 1$). This can be confirmed by the properties of the low-frequency waves, in particular whistler waves [*Tetrick et al*., 2017] or by the direct integration of the electron distributions. Ratio $\omega_p/\omega c$ in the range 10^{-3}–10^{-2}, at most, is consistent with Waves and MAG measurements and estimates from JADE-E. The parameter $\varepsilon = (\omega_p/\omega_c)^2$ is important for the CMI process. Low values of ε place the cutoff frequency of the X mode ($\omega_X = \omega_c\,(1+\varepsilon/2)$) extremely close to ω_c. Such conditions help the relativistic resonance of the electrons and favor the CMI process, as detailed in the next section. Note that the boundaries of the source are not well defined, contrary to the terrestrial AKR case [*Louarn et al*., 1990; *Ergun et al*., 1998].

As seen in Figure 1b, the bulk of the electron population does not exceed a few keV. There is no trace of localized strong electron acceleration during the period 13:28–13:29:45. This is unusual compared to expectations from Earth where the sources of AKR are observed to precisely correspond to the regions of particle acceleration corresponding to the aurora (inverted "V" structures), typically crossed in a few seconds by spacecraft. In the absence of strong acceleration, the CMI would be driven by electrons of modest energy, typically in the range 2–10 keV and apparently more widely spread than at Earth. Incidentally, this also explains why radiation is not seen below f_c: the relativistic correction of f_c is less than 5–10^{-3}, thus below the frequency resolution of Waves survey mode.

The pitch angle distributions in Figure 1 show several interesting features, such as upward and downward beams and a pronounced loss cone in the upward electron population, from about 150 to 180° [see also *Kurth et al*., 2017; *Allegrini et al*., 2017]. The apparent decrease of flux at ~90° is due to spacecraft obstruction [*Allegrini et al*., 2017]. The loss cone is particularly strong from 13:28:00 to 13:29:20, at ~2–6 keV, precisely

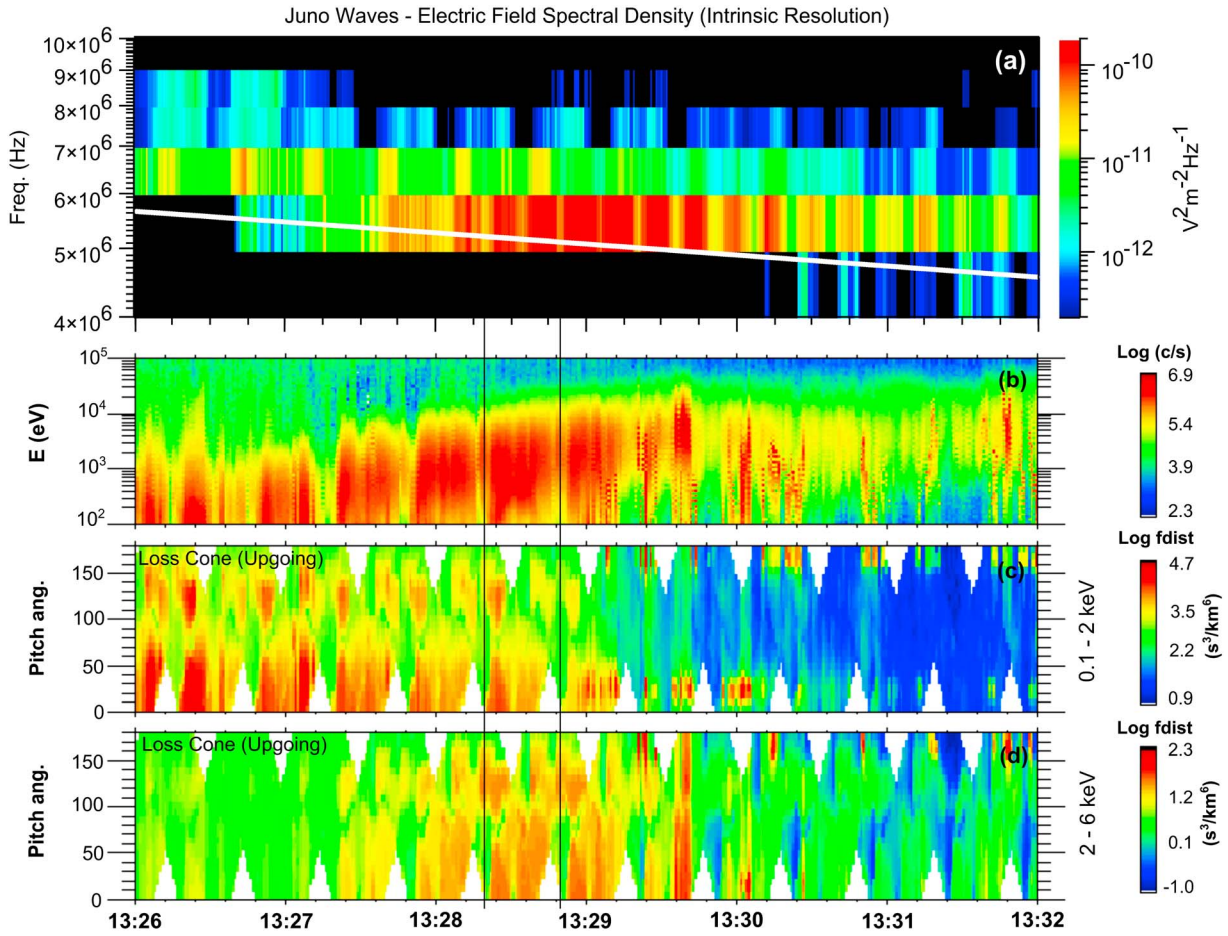

Figure 1. Combined JADE-E and Waves observations obtained near and inside a HOM source. (a) Waves dynamic spectra from 4 to 10 MHz; the white line is the electron gyrofrequency based on the locally measured magnetic field. (b) Time-energy electron flux, from 100 eV to 100 keV. (c and d) Electron pitch angle distributions at 100–2000 eV and 2000–6000 eV (white areas indicate lack of observations). The loss cone is seen at 150–180°. The two vertical lines indicate the times of the selected distributions (see Figure 2).

when the radio flux peaks. Knowing that loss cone electron distributions are the traditional form of free energy used to drive the CMI [*Wu and Lee*, 1979], this observation leads us to investigate whether the observed positive perpendicular gradients of the distribution ($\partial f/\partial v_\perp > 0$) are sufficient to amplify the waves and explain the HOM generation. The observations made in the northern hemisphere during the first crossing of the HOM source (source "B" in *Kurth et al.* [2017]) are very similar. They show no clear trace of particle acceleration and support the case for loss cone distributions being the driver of the CMI process.

Nevertheless, before applying the CMI theory to the loss cone distributions, we point out a possible particle energization at ~13:29:40, crossed in about ~5 s. This short signature is also characterized by a widespread pitch angle distribution, seen in the 2–6 keV panel, with relatively large phase space density at ~90° and for particles moving downward toward the planet. This short signature may be analogous to distributions seen in AKR sources. If more cases are observed on subsequent Juno perijove passes, then this would indicate that different regimes of CMI may coexist and explain the HOM generation.

3. The Cyclotron Maser

We summarize here some important elements of the CMI theory. There is considerable literature on this subject with details provided by *Wu and Lee* [1979], *Wu* [1985], *Le Quéau et al.* [1984a, 1984b], and *Pritchett* [1986]. We skip many developments of the theory to directly present the key elements of the amplification

of *X*-mode waves by the CMI, in close vicinity to the electron gyrofrequency in the case of a low density ($\varepsilon = (\omega_p/\omega_c)^2 \ll 1$) and moderately energetic ($E \ll m_e c^2$) plasma.

As shown, for example, by *Le Quéau et al.* [1984a, 1984b], close to the cutoff (ω_X), *X*-mode waves have a dominant right-handed polarization (the electric field rotates about the ambient magnetic field in the same sense as electrons) and their dispersion equation can be reduced to

$$D = 1 - k^2c^2/\omega^2 + \left(1 - k_\perp^2 c^2/2\omega^2\right)J = 0 \tag{1}$$

where J is linked to the right-handed component of the current and is given by

$$J = \frac{\omega_p^2}{2\omega^2}\int_0^{+\infty} 2\pi p_\perp^2 dp_\perp \int_{-\infty}^{+\infty} dp_\parallel \frac{(\omega - k_\parallel v_\parallel)\partial f/\partial p_\perp + k_\parallel v_\perp \partial f/\partial p_\parallel}{\Gamma(\omega - k_\parallel v_\parallel) - \omega_c}. \tag{2}$$

In this formula, f is the distribution function of the electrons normalized so $\int f\, dp^3 = 1$, $p_{\perp,\parallel}$ are the relativistic momenta of the particles in directions perpendicular and parallel to the magnetic field. $\Gamma = (1 + p^2/m^2c^2)^{1/2} = (1 - v^2/c^2)^{-1/2}$ is the relativistic factor. Note that we use perturbations proportional to $\exp[i(kr - \omega t)]$. For weakly relativistic electrons ${\beta_{\perp,\parallel}}^2 = (v_{\perp,\parallel}/c)^2 \ll 1$ and supraluminous waves ($\omega/k_\parallel \gg c$) propagating close to the gyrofrequency ($\omega \sim \omega_c$), this expression can be simplified to

$$J = 2\pi \frac{\omega_P^2}{\omega_c^2}\int_0^{+\infty} \beta_\perp^2 d\beta_\perp \int_{-\infty}^{+\infty} d\beta_\parallel \frac{\partial f/\partial \beta_\perp}{\left(\beta_\parallel - \beta_0\right)^2 + \beta_\perp^2 - \left(\beta_0^2 - 2\Delta\omega\right)}, \tag{3}$$

with $\beta_0 = k_\parallel c/\omega_c$ and $\Delta\omega = (\omega - \omega_c)/\omega_c$.

The dispersion equation is generally solved by considering that the electron distribution is split into a dominant cold or thermal population (f_0) that supports the wave propagation and a tenuous energetic population (f_b) that feeds the instability. The real part of the current J is then linked to the cold plasma population as

$$J_c = -\omega_{p0}^2/\omega(\omega - \omega_c) \approx -\omega_{p0}^2/\omega_c^2\Delta\omega \tag{4}$$

The imaginary part $\mathrm{Im}(J_b)$ is obtained from f_b by integrating (3) along the resonant curve $\left(\beta_\parallel - \beta_0\right)^2 + \beta_\perp^2 - \left(\beta_0^2 - 2\Delta\omega\right) = 0$. This resonant condition determines a circle in the $(\beta_\perp, \beta_\parallel)$ plane, with center $\beta_\parallel = \beta_0$ and radius $b = \left(\beta_0^2 - 2\Delta\omega\right)^{1/2}$. Using the standard Plemelj formula, $\int_{-\infty}^{+\infty} dz/(Z - z) \equiv PP. + i\pi\delta(Z - z)$, one then gets

$$\mathrm{Im}(J_b) = -\pi^2 \frac{\omega_{Pb}^2}{\omega_c^2}\int_0^{\pi} d\theta b^2 \sin(\theta)^2 \frac{\partial}{\partial\beta_\perp} f_b(\beta_0 + b\,\cos(\theta), b\,\sin(\theta)) \tag{5}$$

The imaginary term involves an integration of the perpendicular gradient of the distribution function along the resonant circle.

The growth rate of the wave is then obtained by a first-order development of D, assuming $\omega = \omega_r + i\gamma$ with $\gamma \ll \omega_r$:

$$\gamma = -\mathrm{Im}(J)(\partial D_c/\partial\omega)^{-1}. \tag{6}$$

Using the expression of the cold plasma current, one has

$$\frac{\partial D_c}{\partial\omega} = \frac{\omega_{p0}^2}{\omega_c^3}\frac{1 - k_\perp^2 c^2/2\omega^2}{\Delta\omega^2}. \tag{7}$$

In so low $(\omega_p/\omega_c)^2$ plasma, it can be shown that *X*-mode waves propagating at frequencies a fraction of a percent above ω_X have an index of refraction very close to 1. The growth rate is then given by

$$\frac{\gamma}{\omega_c} \sim 2\pi^2 \frac{n_b}{n_0}\Delta\omega^2 \int_0^{\pi} d\theta b^2 \sin(\theta)^2 \frac{\partial}{\partial\beta_\perp} f_b(\beta_0 + b\,\cos(\theta), b\,\sin(\theta)), \tag{8}$$

where n_b/n_0 is the ratio of the densities of the energetic and thermal populations.

As shown in equation (8), the condition for wave amplification is the existence of positive $\partial f/\partial v_\perp$ gradients, the most amplified waves being characterized by circles of resonance lying in the phase space region of

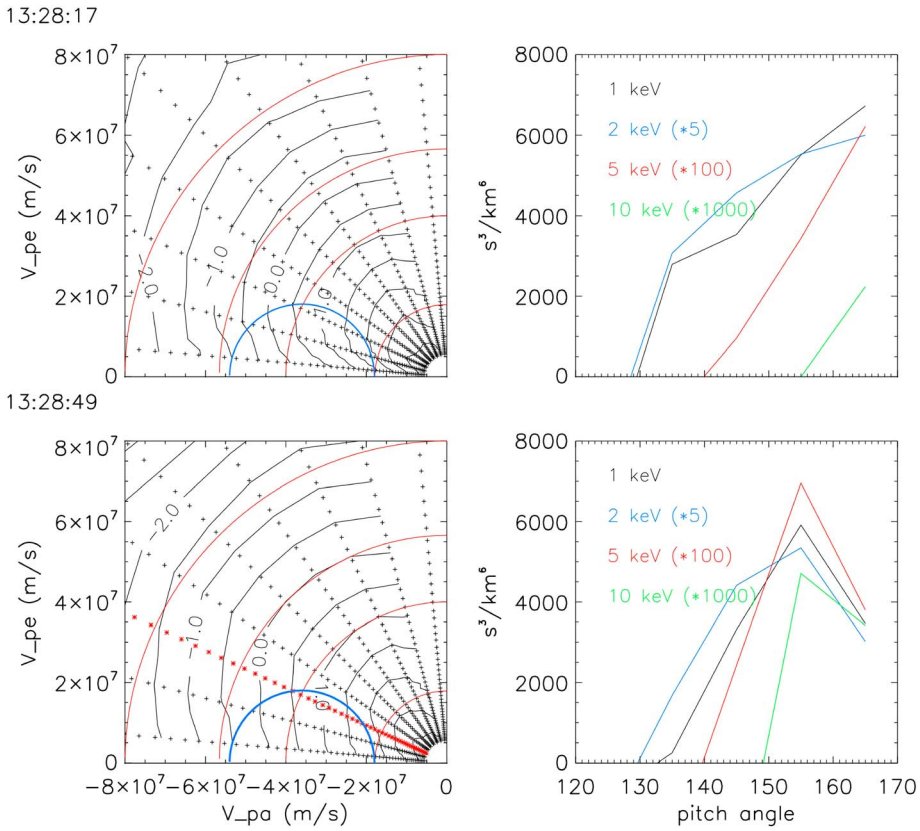

Figure 2. (left column) Distribution of the upgoing electrons at 13:28:17 and 13:28:49. The isocontours are shown using a logarithmic scale in units of s^3/km^6. The red circular arcs correspond to energies of 1, 5, 10, and 20 keV and the radial lines to pitch angles of 175°, 165°, 155°, …. An example of a resonant circle is displayed in blue. (right column) Corresponding $\partial f/\partial v_\perp$ gradients (units of s^3/km^6) at 1, 2, 5, and 10 keV, measured in the loss cone.

maximum positive slope. In the case of loss cone distributions, the waves with maximum amplification propagate upward, at large oblique angles with respect to the static *B* field and at frequencies slightly above f_c.

We note the assumption that two different populations are supposed to coexist, a dominant one that supports the propagation and a tenuous one that drives the maser. The point is in fact more subtle. Theoretically, the difficulty is to evaluate the principal part of the integral in formula (3) when one applies the Plemelj method. In fact, the cold plasma formula (4) can be considered as a first simple evaluation of this principal part, i.e., the real part of *J*, assuming n_b=n_0. In other words, the assumption is equivalent to neglecting the finite temperature effects in the calculation of Re(*D*). The complete formula can be found in *Le Quéau et al*. [1984a] for Maxwellian-type distributions and involves algebraic developments that are beyond the scope of the present simple approach. Nevertheless, we verify that the inclusion of the thermal dispersion effects does not significantly change the dispersion properties of the amplified waves since they propagate with a refractive index close to 1. The use of formula (8), with n_b=n_0, is thus sufficient for a first approach. The complete analysis will be detailed in a future study.

4. Application to the HOM Generation

In Figure 2, the distribution functions of the upgoing electrons measured at ~13:28:17 and 13:28:49 are displayed. The first corresponds to the period of increasing HOM flux (~$3–4\times10^{-11}\,V^2\,m^{-2}\,Hz^{-1}$), the second to the maximum flux ($>10^{-10}\,V^2\,m^{-2}\,Hz^{-1}$). The distribution at 13:28:49 shows larger phase space density at a given energy (the isocontours are enlarged), which corresponds to a denser and hotter plasma. The loss cone is clearly apparent at pitch angles larger than 155°, indicated by the red radial line. In the loss cone, the isocontours do not follow the isoenergy circles (some of which are indicated in red). They are curved

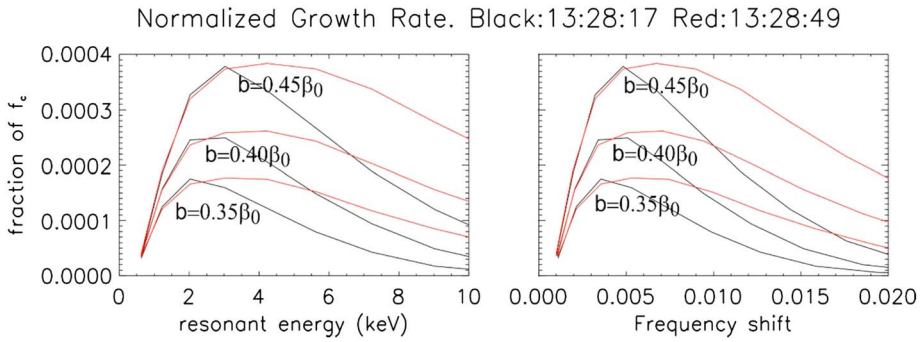

Figure 3. Normalized growth rate (γ/ω_c) obtained from the measured $\partial f/\partial\beta_\perp$. The resonant energy is the energy at the center of the resonant circle (β_0). The frequency shift is given by $\Delta\omega = \left(\beta_0^2 - b^2\right)^{1/2}/2$ (see expression of b in the resonant circle formula, section 3).

toward low energies. This region of phase space is characterized by positive $\partial f/\partial v_\perp$ gradients, given by the term $\cos\alpha\sqrt{m_e/2E}\,\partial f/\partial\alpha$ in energy-pitch angle (E-α) coordinates.

In Figure 2 we also place a resonant circle corresponding to an expected large wave amplification. The center, $v_0 = -3.6\times10^7$ m/s, corresponds to β_0 ~0.12 and E ~4 keV. For waves with index close to 1, β_0 is also the cosine of the angle of propagation with respect to the B field. This propagation angle (ϕ) is ~83° in this case. To have a large circle in the loss cone, we set b (the radius of the circle) to $\beta_0/2$. Using the formula of b, this leads to $\Delta\omega = 3\beta_0{}^2/8$ ~3×10^{-3}. This is above the X-mode cutoff ($\Delta\omega_X = \varepsilon/2$~$10^{-5}$–$10^{-6}$ according to the expected values of ω_p/ω_c). Note also that the wave index is very close to 1 (~0.98–0.99), using formula (1). This example shows the expected characteristics of amplified waves: an angle of propagation a few degrees below 90°, corresponding to the center of the resonant circle at 3–6 keV; the frequency is in the range $\Delta\omega$ ~1–5×10^{-3}, and the resonant circle as a radius between 0.3 and 0.6 β_0, which should optimize the use of the available free energy of the loss cone distribution.

The measured $\partial f/\partial\beta_\perp$ gradients are shown in Figure 2 (right column), for energies ranging from 1 to 10 keV. The second distribution shows positive $\partial f/\partial\beta_\perp$ gradients that extend toward larger energies than the first (see estimates at 5 and 10 keV). Using these measurements, the growth rate is then estimated from formula (8). Note that this formula assumes that f is normalized in the β space ($\int f\,d\beta^3 = 1$). This requires setting the appropriate normalization factor before using the measured $\partial f/\partial\beta_\perp$ gradients that are expressed in s^3/km^6. In practice, the factor is $c^3\ 10^{-18}/n$, where n is the density (in m^{-3}) obtained by integrating f.

The estimated growth rates (γ/ω_c) are shown in Figure 3, for different values of $\beta_0$and b, and thus, different angles of propagation ϕ and frequency shifts $\Delta\omega$. The normalization factor is set with n ~30 cm^{-3}, which most certainly is overestimated and, thus, likely leads to underestimated growths. One gets γ/ω_c larger than 3x10^{-4} for resonant energies in the range 2–5 keV at 13:48:17 and 2–9 keV at 13:28:49. Considering waves with index very close to 1, one has: $\cos(\phi)\approx\beta_0$and $\Delta\omega = \left(\beta_0^2 - b^2\right)^{1/2}/2$ (see section 3). From Figure 3, one can deduce that large amplifications (defined by amplification rates above 80% of the maximum growth) are obtained at propagation angles varying from 85° to 82°at 13:28:17 and 85° to 79° at 13:28:49, over the frequency bandwidth $\Delta\omega$ ~ 3–7×10^{-3} and $\Delta\omega$ ~ 3–14×10^{-3}, respectively. This corresponds to Δf~50 kHz, which is consistent with the high spectral resolution measurements performed in the source [*Kurth et al.*, 2017, Figure 4]. The typical spectral width of amplification is ~0.5–1×10^{-2}. The larger width at 13:28:49 denotes a more instable situation. Note that the values of normalized growth rate are close to those obtained at Earth for similar distribution functions [see *Omidi et al.*, 1984].

The important difference compared with Earth comes from the much larger values of the gyrofrequency at Jupiter. Indeed, since ω_c~$3\times10^7\ s^{-1}$, the growth rate corresponds to a typical e-folding time of 10^{-4}s. This is about a factor 20–30 less than what is obtained at Earth with loss cone distributions. To get intensities of the order of $10^{-10}\ V^2/m^2$ Hz by amplifying the typical radio noise (~$10^{-20}\ V^2\ m^{-2}\ Hz^{-1}$), amplification factors of e^{10} to e^{20} are needed. This corresponds to amplification times of 1–2×10^{-3} s and, thus, amplification length (L) in the range 3–6×10^2 km (say, 1000 km or a few 10^3 wavelengths, with margin). L~1000 km at

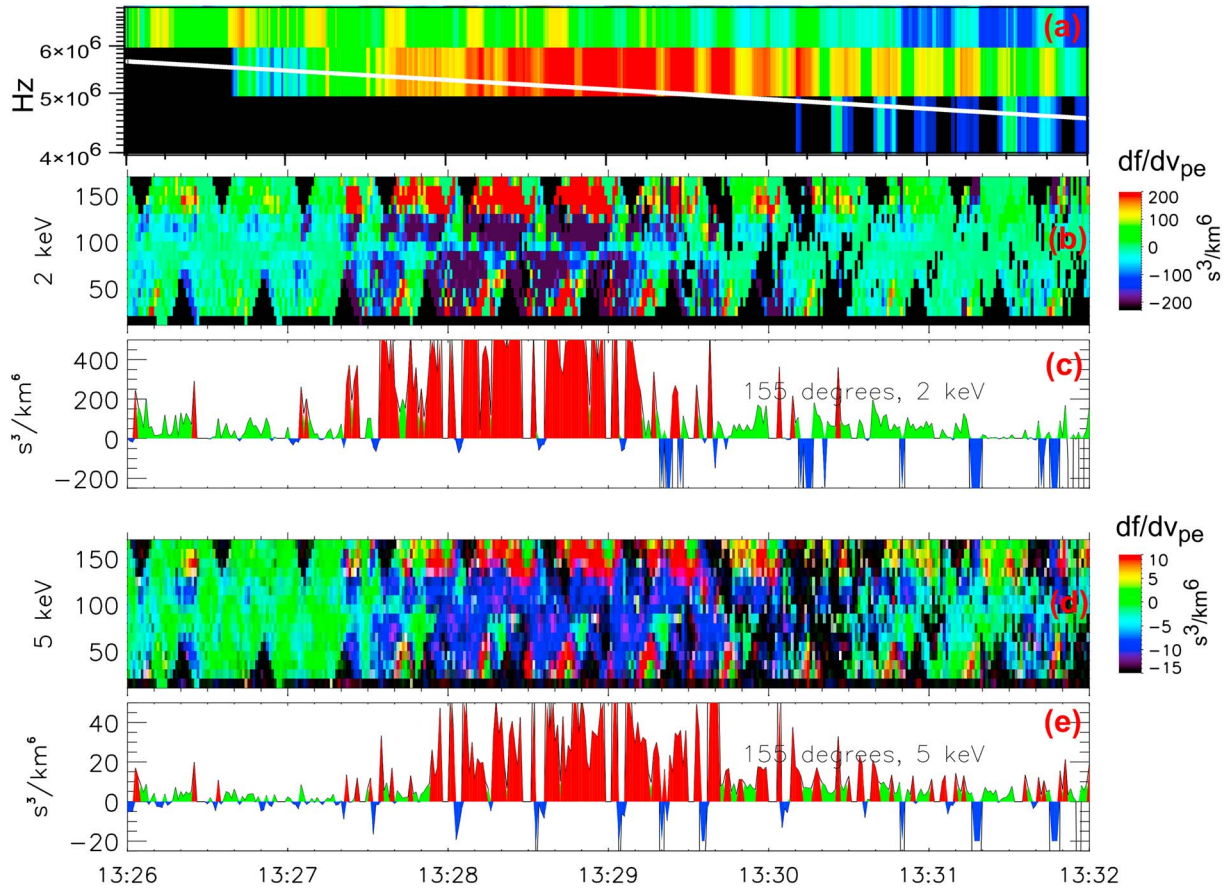

Figure 4. (a) Waves dynamic spectra (as in Figure 1). (b and d) Measured $\partial f/\partial\beta_\perp$ gradients at 2 keV and 5 keV shown in pitch angle plots. (c and d) Gradients at 155° in units of s^3/km^6. The red regions correspond to values above the CMI thresholds (see text).

very oblique propagation (83°) represents a propagation Δh~100 km in altitude. Over this altitude range, the gyrofrequency varies by ~2×10^{-3} ($\Delta f_c/f_c \sim 3\,\Delta h/R$, where R~1.6 R_J is the distance from Jupiter center) which is smaller than the spectral width of amplification. This guarantees an optimal growth over the whole path. Our conclusion is that the estimated CMI growth rates are sufficient to explain the HOM generation.

5. Discussion and Conclusion

Having shown from specific electron distribution functions that the loss cone seems sufficient to drive the CMI and explain the HOM generation, it is interesting to understand the generality of this result. We reverse the reasoning to estimate the minimum $\partial f/\partial\beta_\perp$ gradients that would be needed to explain the HOM generation. The maximum possible amplification path can be estimated from the spectral width of the instability. Taking a width of 10^{-2}, one gets Δh~250 km, for R~ 1.6 R_J. For propagation at 83°, this leads to a maximum amplification path of ~2500 km. For larger paths, the waves leave the amplification spectral domain due to the variation of f_c. To have an amplification by e^{10-20} over this distance, e-folding times of 5×10^{-4}–10^{-3} s are required. This is a factor 5 more than our previous estimates and basically means that $\partial f/\partial\beta_\perp$ gradients 5 times less than those observed at 13:28:17 and 49 would still be sufficient to drive the CMI (for comparable plasma density and gyrofrequency). We conclude that gradients $\partial f/\partial\beta_\perp$ of the order of 100–200 s^3/km^6 at 2 keV and 10 s^3/km^6 at 5 keV would be sufficient to explain the HOM generation.

We consider these thresholds in Figure 4. We calculate the $\partial f/\partial\beta_\perp$ gradients at 2 keV and 5 keV. They are shown in pitch angle format. The red color corresponds to $\partial f/\partial\beta_\perp$ gradients larger than the thresholds, thus 200 s^3/km^6 (2 keV) and 10 s^3/km^6 (5 keV). These large gradients are mostly seen from 13:27:40 to 13:29:20, in the loss cone, when the wave flux is maximum.

More precisely, the wave intensity starts to increase at 13:27:40, precisely when the large gradients also start to be observed at 2 keV. However, the maximum wave intensity is observed a few tens of seconds later, from 13:28:10 to 13:29:20, when the large gradients are also observed at 5 keV. This is coherent with Figures 2 and 3 showing that the distribution at 13:28:49 presents larger slopes at 5–10 keV than the one at 13:28:17 which, in overall, is a sign of a more unstable situation. This also suggests that the population at 5–10 keV would be the main driver of the CMI.

To conclude, we analyze the first example of a spacecraft making direct measurements while crossing Jupiter's HOM source region. We show that the radio emission mechanism, the CMI, is driven by loss cone distributions. The CMI *e*-folding time of 10^{-4}s that is estimated from the electron distributions measured by JADE-E is indeed sufficient to explain the HOM intensity measured by Waves, the main free energy of the CMI being associated with electron populations at 5–10 keV. Additional observations and more detailed analysis are needed to better evaluate the finite temperature effects on the CMI and firmly established the scenario of HOM generation. At present, there is no indication that a similar scenario would be applicable at decametric or kilometric wavelength (DAM and KOM radiations).

Acknowledgments
We would like to thank all the outstanding women and men who have made JADE, Waves, MAG, and Juno a reality. P. Louarn expressed his strong gratitude to JADE team and especially, D. McComas, for offering the opportunity to participate to this extraordinary investigation. He also thanks J. Rouzaud and E. Penou, the latter greatly helping with the particle analysis through the CL software. The French part of this works is supported by CNRS and CNES. The research at the University of Iowa was supported by NASA through contract 699041X with Southwest Research Institute. The JNO-J/SW-JAD-3-CALIBRATED-V1.0 and JNO-J/SW-JAD-2-UNCALIBRATED-V1.0 data sets were obtained from the Planetary Data System (PDS) at http://pds.nasa.gov/.

References

Allegrini, F., et al. (2017), Electron beams and loss cones in the auroral regions of Jupiter, *Geophys. Res. Lett.*, doi:10.1002/2017GL073180, in press.
Bagenal, F., et al. (2014), Magnetospheric science objectives of the Juno mission, *Space Sci. Rev.*, doi:10.1007/s11214-014-0036-8.
Burke, B. F., and K. L. Franklin (1955), Observations of a variable radio source associated with the planet Jupiter, *J. Geophys. Res.*, *60*(2), 213–217, doi:10.1029/JZ060i002p00213.
Connerney, J. E. P., et al. (2017), The Juno magnetic field investigation, *Space Sci. Rev.*, doi:10.1007/s11214-017-0334-z.
Delory, G. T., R. E. Ergun, C. W. Carlson, L. Muschietti, C. C. Chaston, W. Peria, J. P. McFadden, and R. Strangeway (1998), FAST observations of electron distributions within AKR source regions, *Geophys Res Lett*, *25*(12), 2069–2072, doi:10.1029/98GL00705.
Ergun, R. E., et al. (1998), FAST satellite wave observations in the AKR source region, *Geophys. Res. Lett.*, *25*(12), 2061–2064, doi:10.1029/98GL00570.
Kurth, W. S., et al. (2017), A new view of Jupiter's auroral radio spectrum, *Geophys. Res. Lett.*, doi:10.1002/2017GL072889, in press.
Lamy, L., et al. (2010), Properties of Saturn kilometric radiation measured within its source region, *Geophys. Res. Lett.*, *37*, L12104, doi:10.1029/2010GL043415.
Le Quéau, D., and P. Louarn (1989), Analytical study of the relativistic dispersion: Application to the generation of the auroral kilometric radiation, *J. Geophys. Res.*, *94*(A3), 2605–2616, doi:10.1029/JA094iA03p02605.
Le Quéau, D., R. Pellat, and A. Roux (1984a), Direct generation of the auroral kilometric radiation by the maser synchrotron instability—An analytical approach, *Phys. Fluids*, *27*, 247–265, doi:10.1063/1.864520.
Le Quéau, D., R. Pellat, and A. Roux (1984b), Direct generation of the auroral kilometric radiation by the maser synchrotron instability: Physical mechanism and parametric study, *J. Geophys. Res.*, *89*(A5), 2831–2841, doi:10.1029/JA089iA05p02831.
Louarn, P., A. Roux, H. deFéraudy, D. Le Quéau, M. André, and L. Matson (1990), Trapped electrons as a free energy source for the auroral kilometric radiation, *J. Geophys. Res.*, *95*(A5), 5983–5995, doi:10.1029/JA095iA05p05983.
McComas, D. J., et al. (2013), The Jovian Auroral Distributions Experiment (JADE) on the Juno Mission to Jupiter, *Space Sci. Rev.*, 1–97.
Melrose, D. B., and G. A. Dulk (1982), Electron-cyclotron masers as the source of certain solar and stellar radio bursts, *Astrophys. J. Part 1*, *259*, 844–858, doi:10.1086/160219.
Omidi, N., C. S. Wu, and D. A. Gurnett (1984), Generation of auroral kilometric and *Z* mode radiation by the cyclotron maser mechanism, *J. Geophys. Res.*, *89*(A2), 883–895, doi:10.1029/JA089iA02p00883.
Pritchett, P. L. (1986), Cyclotron maser radiation from a source structure localized perpendicular to the ambient magnetic field, *J. Geophys. Res.*, *91*(A12), 13,569–13,581, doi:10.1029/JA091iA12p13569.
Roux, A., A. Hilgers, H. Deferaudy, D. Lequeau, P. Louarn, S. Perraut, A. Bahnsen, M. Jespersen, E. Ungstrup, and M. Andre (1993), Auroral kilometric radiation sources—In-situ and remote observations from Viking, *J. Geophys. Res.*, *98*(A7), 11,657–11,670, doi:10.1029/92JA02309.
Szalay, J. R., et al. (2017), Plasma measurements in the Jovian polar region with Juno/JADE, *Geophys. Res. Lett.*, doi:10.1002/2017GL072837, in press.
Tetrick, S. S., D. A. Gurnett, W. S. Kurth, M. Imai, G. B. Hospodarsky, S. J. Bolton, J. E. P. Connerney, S. M. Levin, and B. H. Mauk (2017), Plasma waves in Jupiter's high latitude regions: Observations from the Juno spacecraft, *Geophys. Res. Lett.*, *44*, doi:10.1002/2017GL073073, in press.
Wu, C. S. (1985), Kinetic cyclotron and synchrotron maser instabilities—Radio-emission processes by direct amplification of radiation, *Space Sci. Rev.*, *41*(3–4), 215–298.
Wu, C. S., and L. C. Lee (1979), A theory of the terrestrial kilometric radiation, *Astrophys. J.*, *230*, 621–626, doi:10.1096/157120.
Zarka, P. (1998), Auroral radio emissions at the outer planets: Observations and theories, *J. Geophys. Res.*, *103*(E9), 20,159–20,194, doi:10.1029/98JE01323.